KeAi
CHINESE ROOTS
GLOBAL IMPACT

Available online at www.keaipublishing.com/en/journals/journal-of-magnesium-and-alloys/

ScienceDirect

Journal of Magnesium and Alloys 17 (2026) 102033

www.elsevier.com/locate/jma

Full Length Article

Synthesis of sulfur self-doped FeNi–S coordinated carbon derived from petroleum coke for accelerated Mg/MgH_2 hydrogen storage

Yulin Huang[a], Fenghua Wei[b], Yang Zhang[a], Xinan Zhang[c], Yiming Wang[a], Chen Huang[a], Yuke Li[d], Jingcai Chang[a,e,*]

[a] School of Environmental Science and Engineering, Shandong University, Qingdao, Shandong 266237, China
[b] Assets and Laboratory Management Office, Shandong University, Qingdao, Shandong 266237, China
[c] Green Hydrogen Division, Qingda Low Carbon Green Hydrogen Industrial Technology Research Institute (Qingdao) Co., LTD, Qingdao, China
[d] Department of Water Management, Faculty of Civil Engineering and Geosciences, Delft University of Technology, Stevinweg 1, 2628 CN Delft, Netherlands
[e] WeiHai Research Institute of Industrial Technology, Shandong University, Weihai, Shandong 264209, China

Received 22 November 2025; received in revised form 22 January 2026; accepted 18 February 2026
Available online 18 March 2026

Abstract

Interactions between metals and heteroatom-coordinated sites on the carbon matrix are crucial for enhancing the kinetics and thermodynamics of Mg/MgH_2. Herein, we reported a sustainable K_2FeO_4 activation strategy that converts high-sulfur petroleum coke into a sulfur self-doped porous carbon hosting FeNi–S coordinated active sites. Tailoring the alloyed electronic structure and exposing more catalytically active sites substantially enhanced the hydrogenation and dehydrogenation kinetics of Mg/MgH_2 with (FeNi)S@PPC. Its peak dehydrogenation temperature was 95.39 °C lower than that of ball-milled MgH_2. In addition, it enabled MgH_2 to release 4.89 wt.% H_2 within 20 min at 275 °C, exceeding its sulfur-free counterpart (FeNi)@PPC by 1.41 wt.%. Moreover, the (FeNi)S@PPC/MgH_2 showed 99.5% capacity retention after 30 cycles, indicating excellent reversibility. Mechanistic investigations revealed that intrinsic sulfur self-doping induced a stable FeNi–S coordination environment, which lowered the D-band center of FeNi to −1.349 eV. The electronic redistribution was found to weaken the FeNi–(H) intermediate, lowering the dissociation and diffusion energy barrier by 0.39 eV and facilitating hydrogenation. This also reduced the energy required for Mg–H dissociation into H_2 by 0.65 eV. Consequently, the dehydrogenation activation energy was decreased to 97.09 $kJ{\cdot}mol^{-1}$, with the rate-limiting step shifting to a low-energy barrier three-dimensional interfacial reaction (R3 model). Overall, this study establishes a green valorization route for high-sulfur petroleum coke and elucidates a fundamental metal–sulfur charge transfer mechanism that substantially enhances magnesium-based hydrogen storage.

Keywords: MgH_2; FeNi–S coordination; Hydrogen absorption/desorption kinetics; Sulfur self-doping; Catalytic mechanism.

1. Introduction

Hydrogen energy is emerging as a pivotal force in the green and low-carbon transformation of energy systems [1–4]. Projections from the International Energy Agency in its "Global Hydrogen Review 2024" indicate that hydrogen energy is expected to constitute 12% of the global final energy consumption by 2050. Consequently, the advancement of efficient and safe hydrogen storage technologies is strategically essential for establishing a clean and secure national energy system [5,6]. Solid-state storage methodologies using metal hydrides are particularly noteworthy due to their high theoretical hydrogen storage capacities and moderate hydrogen pressure requirements [7,8]. The binary metal hydride MgH_2 represents a promising hydrogen storage material because of its abundance and high hydrogen density (7.6 wt.%) [9]. However, the practical application of MgH_2 is limited by its high reaction enthalpy, the considerable dissociation energy of H_2, and the strong Mg–H bonds, which collectively lead to elevated desorption temperatures and activation energies [10–13].

Peer review under the responsibility of Chongqing University.
* Corresponding author.
E-mail address: changjingcai@sdu.edu.cn (J. Chang).

https://doi.org/10.1016/j.jma.2026.102033

Nomenclature

BET	Brunauer–Emmett–Teller
CI-NEB	Climbing image nudged elastic band
COHP	Crystal orbital Hamilton population
D-HSPC	Desulfurized high-sulfur petroleum coke
DFT	Density functional theory
DOS	Density of states
DSC	Differential scanning calorimetry
EDS	Energy-dispersive X-ray spectroscopy
(FeNi)@G	FeNi bimetallic alloy supported on graphite
(FeNi)@Gr	FeNi bimetallic alloy supported on graphene
(FeNi)@PPC	FeNi bimetallic alloy supported on petroleum porous activated carbon without sulfur self-doping
(FeNi)S@PPC	Sulfur self-doped FeNi bimetallic alloy supported on petroleum porous activated carbon
(FeO)S@PPC	Sulfur self-doped iron oxide supported on petroleum porous activated carbon
(FeTM)S@PPC	Sulfur self-doped FeTM alloy (TM = Cr, Mn, Co, Ni, or Cu) supported on petroleum porous activated carbon
(FeTM)S@PPC/MgH_2	MgH_2 composite catalyzed by (FeTM)S@PPC
HRTEM	High-resolution transmission electron microscopy
HSPC	High-sulfur petroleum coke
PCT	Pressure–composition–temperature
PDOS	Partial density of states
SAED	Selected area electron diffraction
SEM	Scanning electron microscopy
TPD	Temperature-programmed desorption
VASP	Vienna Ab initio Simulation Package
XPS	X-ray photoelectron spectroscopy
XRD	X-ray diffraction

The hydrogen storage performance of MgH_2 can be enhanced by the addition of transition metal (TM) dopants [14–19]. These additional components interact with Mg/MgH_2 to facilitate hydrogen absorption and release, through interface effects, alloy phase formation during cycling, and the provision of catalytically active sites [20–22]. Furthermore, the catalytic performances of TM dopants are influenced not only by the metal itself, but also by the nature of the support and the impact of metal–support interactions [19,23]. For example, Guan et al. [14] demonstrated that doping Ti into the MgO lattice and optimizing its valence state to yield stable Ti^{3+} significantly enhanced the hydrogen absorption/desorption kinetics and stable cycling performance. Zhang et al. [19] designed $Ni_{0.034}@TiO_2$ with single-atom Ni supported on TiO_2 via a strong metal-support interaction, which maintained thermal stability and catalytic activity at high temperatures while retaining a 97.26% capacity rate after 100 cycles.

Carbon supports possess distinctive physicochemical properties and advantages in electron modulation compared to oxide supports, rendering them preferred choices for numerous catalytic applications [24,25]. Typically, heteroatoms (N, P, S, B, etc.) on carbon materials were used as anchoring sites for metal nanoparticles, which can significantly influence the electronic structure of the metals through interfacial electron transfer [24,26,27]. Duan et al. [28] recently developed a method for assembling single Mo atoms on N-doped carbon nanotubes (N–CNTs), reducing the Mg hydrogenation activation energy to 21.2 $kJ{\cdot}mol^{-1}$. The excellent hydrogenation kinetics were primarily due to coordination between single Mo atoms and adjacent N atoms on the CNTs, thereby generating half-filled orbital states on the Mo atoms. Additionally, Wang et al. [29] used a hydrothermal method to synthesize N-doped Nb_2O_5 nanorods induced by graphene, which reduced the desorption temperature by 130 °C compared to that of pure MgH_2. Theoretical analysis confirmed that the synergistic effect between the Nb–N–O species and graphene effectively lengthened the Mg–H bond while weakening the H–H bond. However, complex synthesis processes and reliance on expensive carbon precursors restrict the scalable application of the produced catalysts.

High-sulfur petroleum coke (HSPC), a byproduct of crude oil refining with a carbon content above 80% and a bulk sulfur content of 3–10%, serves as an excellent candidate for fabricating sulfur-doped carbon supports. In this work, we developed an eco-friendly method to transform HSPC into sulfur self-doped carbon catalysts (FeTM)S@PPC, with potential for large-scale applications. Green oxidant K_2FeO_4 was employed as a substitute for traditional potent base activators (such as KOH) for HSPC, thereby eliminating environmentally harmful post-treatment steps while directly introducing an iron precursor that can alloy with the second active metal. The mild reaction condition promoted the formation of a local coordination microenvironment between sulfur in HSPC and metallic atoms. (FeNi)S@PPC was identified as exhibiting superior performance for enhancing Mg/MgH_2 hydrogen storage. The catalytic evaluations and mechanism study proved that stable

FeNi–S coordination effectively reconstructed the electronic structure of FeNi active sites and weakened the strength of FeNi–(H) intermediate and the Mg–H bonds, thereby enhancing the thermodynamics and kinetics of MgH_2. Overall, this study presents a novel green strategy for the utilization of HSPC solid waste and provides insights into how the local metal–sulfur coordination environment influences the performance of Mg/MgH_2, which could lead to the development of novel hydrogen storage materials.

2. Materials and methods

2.1. Catalyst and hydrogen storage material preparation

HSPC solid waste (86.78 wt.% C, 3.54 wt.% H, 1.33 wt.% O, 0.96 wt.% N, and 7.40 wt.% S) was utilized as both the carbon and sulfur sources, along with K_2FeO_4 as a green activating agent and metal chlorides as the secondary metal sources to synthesize the desired (FeTM)S@PPC materials. For example, considering (FeNi)S@PPC, the synthetic process was performed as follows. HSPC (1 g), K_2FeO_4 (1 g), and anhydrous $NiCl_2$ (0.654 g) were mixed by high-energy mechanical ball milling at a ball-to-powder ratio of 50:1 and a rotational speed of 450 rpm for 8 h to form a highly dispersed bimetallic alloy precursor. The mixture was then placed in a nickel boat and heated to 800 °C under an Ar atmosphere at 5 °C·min^{-1}. Subsequently, the atmosphere was changed to H_2 and maintained for 2 h before cooling. Finally, the product was washed with deionized water to remove any byproducts and dried to obtain the desired (FeNi)S@PPC. The control systems, (FeNi)@PPC and (FeO)S@PPC, were synthesized following the same procedure, except that the HSPC was either desulfurized or did not include a nickel source. Desulfurization of the HSPC was achieved through thermal treatment at 1400 °C for 2 h to ensure the complete removal of intrinsic bulk-phase sulfur. The synthesis procedures for the other catalyst systems were also provided in the Supplementary Information.

(FeTM)S@PPC and MgH_2 were then ball-milled together at a mass ratio of 1:9 to produce the (FeTM)S@PPC/MgH_2 composite hydrogen storage material, maintaining a ball-to-powder ratio of 50:1 and using a rotational speed of 450 rpm for 6 h. Notably, a 10 min break was implemented after each 30 min to avoid overheating and cold welding. The decision to incorporate a 10% catalyst was based on a comprehensive balance between catalytic efficiency and hydrogen storage capacity, a conclusion widely supported by previous studies [29]. Characterization of the structural and surface chemical properties was carried out using X-ray diffraction (XRD, Miniflex 600, Rigaku, Japan), nitrogen adsorption–desorption analysis (ASAP 2460, Micromeritics, USA), X-ray photoelectron spectroscopy (XPS, K-Alpha, Thermo Fisher Scientific, USA), and high-resolution transmission electron microscopy (HRTEM, Talos F200X, FEI, USA); additional experimental details are provided in the Supplementary Information.

2.2. Evaluation of hydrogen absorption/desorption properties

The catalytic performance of (FeTM)S@PPC was evaluated through simultaneous thermogravimetric analysis, non-isothermal and isothermal hydrogen absorption and desorption testing, pressure-composition-temperature (PCT) measurements, and cycling performance assessments. To measure the dehydrogenation peaks and apparent dehydrogenation activation energies of the hydrogen storage materials, differential scanning calorimetry (DSC, Netzsch STA449 F5) was performed under a high-purity Ar protective atmosphere, with a heating rate of 5–20 °C·min^{-1} from room temperature to 550 °C. Non-isothermal hydrogen absorption and desorption tests were conducted using a high-pressure gas adsorption apparatus (TPD, BSD-PHE) at heating rates of 2 and 5 °C·min^{-1}, respectively. The isothermal hydrogen absorption/desorption kinetics, PCT curves, and cycling performance tests were examined using an automated Sievert-type adsorption apparatus (PCT, Setaram GASPRO). The formulas used to calculate the thermodynamic enthalpies and activation energies of hydrogen adsorption and desorption were described in the Supplementary Information.

2.3. Density functional theory (DFT) calculations

DFT calculations were performed using the Vienna Ab initio Simulation Package (VASP 5.4.4) [30–32]. To reveal the crucial role of the FeNi–S coordination in charge transfer and the promotion of the hydrogen absorption/desorption processes, (FeNi)S@PPC, (FeNi)@PPC, and (FeO)S@PPC were examined by loading (FeNi) and (FeO) clusters on sulfur-doped and undoped carbon, respectively. The charge transfer mechanism, density of states (DOS), and crystal orbital Hamilton population (COHP) properties were evaluated after calculating the stable adsorption of H_2 and MgH_2 clusters on the substrate model. The climbing image nudged elastic band (CI-NEB) method was employed to compute the reaction pathways and energy barriers [33]. The plane-wave cutoff energy was set to 450 eV, with energy and force convergence criteria of 1×10^{-5} eV/atom and 0.02 eV/Å, respectively. Additional key details regarding the computational parameters, adsorption energies, and differential charge densities were provided in the Supplementary Information.

3. Results and discussion

3.1. Straightforward synthesis of (FeNi)S@PPC from HSPC and comprehensive advantages

The majority of previously reported functional carbons derived from HSPC are prepared using potent alkaline-activating agents, such as KOH. However, such strong bases can react with the intrinsic bulk-phase sulfur at high temperatures, leading to the formation of low-value sulfates and corrosive gases such as SO_2 and H_2S. The uncontrolled transformation of these sulfur species can inherently disrupt morphology, pose potential environmental pollution risks, and yield low-value

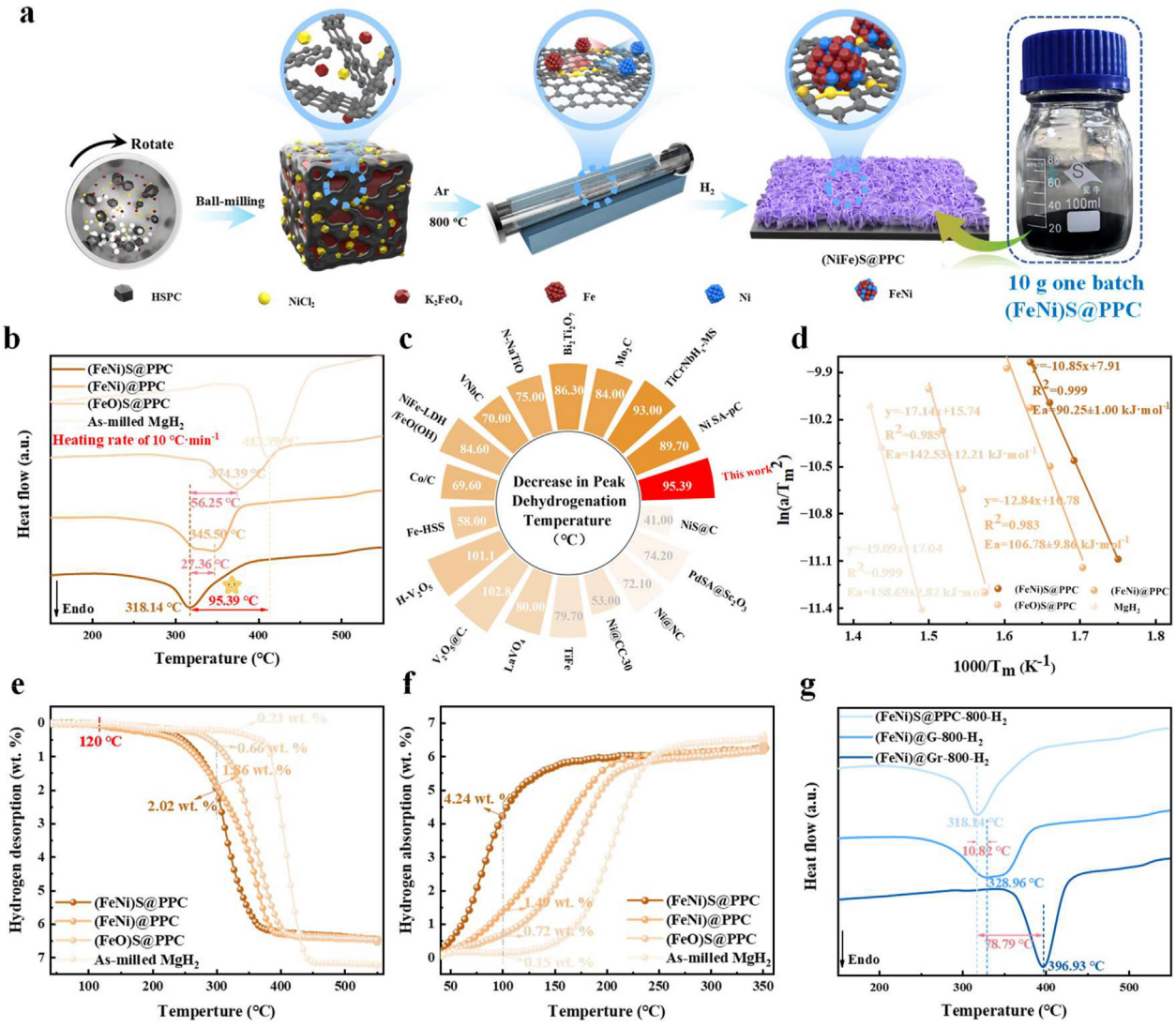

Fig. 1. (a) Schematic representation of the synthetic procedure. (b) DSC curves recorded at a heating rate of 10 °C·min^{-1}. (c) Comparison of the reduction in peak dehydrogenation temperature with literature reports [34–50]. (d) The apparent activation energies of (FeNi)S@PPC, (FeNi)@PPC, (FeO)S@PPC, and ball-milled MgH_2. (e, f) Non-isothermal hydrogen desorption and absorption curves. (g) Catalytic performance comparisons of (FeNi)S@PPC, (FeNi)@G, and (FeNi)@Gr.

carbonized products. In contrast, our green K_2FeO_4 activation strategy effectively avoids the use of strong alkalis and converts bulk sulfur into catalytically active species, thereby preventing sulfur loss and mitigating potential environmental pollution.

Fig. 1a illustrates the schematic representation of the (FeNi)S@PPC synthetic process from HSPC, K_2FeO_4, and $NiCl_2$, which outlines the three main steps, namely high-energy ball milling to form a highly dispersed precursor mixture, decomposition and transformation of the active precursors, and high-temperature reduction to accomplish sulfur self-doping and the solid-state diffusion alloying of Fe with the Ni. Notably, the synthesis of (FeNi)S@PPC yielded ~10 g of catalyst per batch under laboratory conditions, demonstrating its significant potential for scale-up. Based on laboratory-scale estimation, the cost of synthesizing 1 kg of (FeNi)S@PPC was approximately 1106 RMB (Table S1), and this cost is expected to decrease further upon scale-up. Introducing Ni effectively suppresses the oxidation of Fe into Fe_3O_4, thereby enabling the formation of FeNi solid solutions that account for the improved catalytic activity. The product synthesized without the $NiCl_2$ was denoted as (FeO)S@PPC. Meanwhile, desulfurized HSPC was employed following the same procedure to prepare (FeNi)@PPC. As shown in the XRD patterns (Fig. S1), both (FeNi)S@PPC and (FeNi)@PPC exhibit characteristic diffraction peaks of FeNi at 2θ values of 43.71, 50.90, and 74.84°, whereas (FeO)S@PPC predominantly crystallizes as Fe_3O_4, due to the easy oxidation of metallic Fe upon exposure to air.

DSC curves are commonly used to quantitatively characterize the peak dehydrogenation temperature and the apparent activation energy of magnesium-based hydrogen storage materials, serving as essential indicators of their hydrogen storage performance. As shown in Fig. 1b, at a heating rate of

10 °C·min^{-1}, the dehydrogenation peak temperature of MgH_2 catalyzed by (FeNi)S@PPC is 95.39 °C lower than that of ball-milled MgH_2. The (FeNi)@PPC exhibits a higher peak temperature by 27.36 °C compared with (FeNi)S@PPC, while (FeO)S@PPC shows a significantly increased peak temperature of 374.39 °C. It is worth noting that the dehydrogenation peak temperature can be meaningfully used to evaluate improvements in hydrogen storage performance only when referenced against pristine MgH_2. Therefore, as shown in Fig. 1c and Table S2, our results are compared with representative literature data reported in recent years. The results demonstrate that the catalytic performance of this work is comparable to that of some advanced catalysts reported in recent studies. Moreover, owing to the use of a low-cost carbon–sulfur precursor derived from HSPC and an environmentally benign synthesis route, this system exhibits greater potential for applications. Combining the DSC curves (Fig. S2) recorded at heating rates of 5, 10, 15, and 20 °C·min^{-1} with the Kissinger method, the apparent activation energies (Fig. 1d) of (FeNi)S@PPC, (FeNi)@PPC, and (FeO)S@PPC were calculated to be 90.25, 112.90, and 142.53 kJ·mol^{-1}, respectively. Furthermore, as shown in Fig. S3, carbon materials synthesized using KOH as an activator with $FeCl_3$/$NiCl_2$ metal precursors exhibited a MgH_2 dehydrogenation peak temperature of 326.11 °C, confirming the intrinsic advantages of K_2FeO_4 in the functionalization of HSPC for catalyzing the dehydrogenation of MgH_2. The non-isothermal dehydrogenation profiles recorded at 5 °C·min^{-1} (Fig. 1e) illustrated that when the temperature reached 300 °C, (FeNi)S@PPC achieved a dehydrogenation capacity of 2.02 wt.%, markedly surpassing the capacities of (FeNi)@PPC (1.86 wt.%) and (FeO)S@PPC (0.66 wt.%). The non-isothermal hydrogenation process (Fig. 1f) demonstrated the superior low-temperature hydrogenation performance of (FeNi)S@PPC, as evidenced by the fact that it initiated absorption below 50 °C and achieved a capacity of 4.24 wt.% by 100 °C.

A series of experiments was conducted to determine the optimal carbonization conditions by controlling the temperature and atmosphere. The prepared samples were denoted as (FeNi)S@PPC-T-Ar/H_2, where T represents the temperature of the high-temperature reduction treatment. Fig. S4 showed the DSC curves of the MgH_2 dehydrogenation reaction catalyzed (FeNi)S@PPC-T-Ar/H_2. The results indicated that the (FeNi)S@PPC sample obtained under a H_2 atmosphere exhibited a more pronounced catalytic dehydrogenation activity. Notably, the peak dehydrogenation temperature of (FeNi)S@PPC-800-H_2 was 18.95 °C lower than that for the (FeNi)S@PPC-800-Ar. Additionally, the effect of heat-treatment temperature on catalytic performance was primarily attributed to differences in the specific surface areas of the materials, as illustrated in Fig. S5. Although (FeNi)S@PPC-800-Ar has a larger surface area than (FeNi)S@PPC-700-Ar, its higher dehydrogenation temperature may arise from aggregation of FeNi species during the higher-temperature treatment, which reduces the density of accessible active sites. This further underscores the necessity of H_2 treatment, which effectively suppresses FeNi aggregation and enhances dispersion, enabling (FeNi)S@PPC-800-H_2 to combine a high surface area with abundant active sites and exhibit superior catalytic performance. The N_2 adsorption–desorption isotherms indicated that all samples exhibited type IV characteristics with H3 hysteresis loops, and the optimal surface area and pore structure ensured sufficient exposure of catalytically active sites at 800 °C.

To demonstrate the unique advantages of HSPC as a carbon precursor, the catalytic performance of (FeNi)S@PPC was compared with that of the (FeNi)@G and (FeNi)@Gr catalysts, which were prepared under identical conditions using commercial carbon materials (graphene from Sigma-Aldrich and graphite from Shanghai Aladdin) as supports. The XRD patterns recorded for the (FeNi)@G and (FeNi)@Gr catalysts (Fig. S6) revealed the characteristic crystalline phases of the FeNi alloy in addition to the respective diffraction peaks of the corresponding carbon materials. As shown in Fig. 1g, the peak dehydrogenation temperature achieved using the (FeNi)S@PPC catalyst is 10.82 and 78.79 °C lower than that of the (FeNi)@G and (FeNi)@Gr systems. Furthermore, this temperature was lower than the peak dehydrogenation temperature of 327 °C reported by Fu et al. [34] for NiFe@CNT. The performance enhancement may originate from the bulk-phase sulfur inherent to HSPC, which spontaneously migrates to the surface and incorporates into the carbon matrix during carbonization. This resulting sulfur self-doping modifies the electronic structure of the carbon support and consequently regulates the chemical states of FeNi, as demonstrated in the following analysis.

3.2. Structure and electronic properties of the (FeNi)S@PPC

The significant performance advantages exhibited by (FeNi)S@PPC stem from the optimized electronic properties of FeNi by sulfur self-doping on the carbon support. XPS, XRD, SEM, and TEM analyses were employed in conjunction with DFT calculations to elucidate these structure–property relationships. The XPS profiles of the HSPC and its desulfurized counterpart (D-HSPC) are shown in Fig. 2a. It was evident that the sulfur content of the desulfurized petroleum coke retained only 0.56 wt.%, providing a basis for investigating the significant role of sulfur in modulating the metal–support interactions. XRD analysis (Fig. 2b) revealed that H_2 treatment promoted FeNi solid-solution formation at high temperatures and suppressed Fe_3O_4 generation, as evidenced by the sharper FeNi diffraction peaks compared with those from samples treated under an Ar atmosphere. The microstructure of (FeNi)S@PPC (Fig. 2c) consisted of a uniformly distributed layered array of FeNi on the carbon matrix surface, thereby exposing more catalytically active sites. Similarly, as shown in Fig. S7a–b, (FeNi)@PPC also exhibited well-ordered FeNi arrays, thereby excluding morphological effects on hydrogen storage performance. The TEM and energy-dispersive X-ray spectroscopy (EDS) results in Fig. 2d–f confirmed the uniform distributions of Ni, Fe, and S throughout the carbon matrix. High-resolution TEM (HRTEM) analysis revealed lattice fringes with measured in-

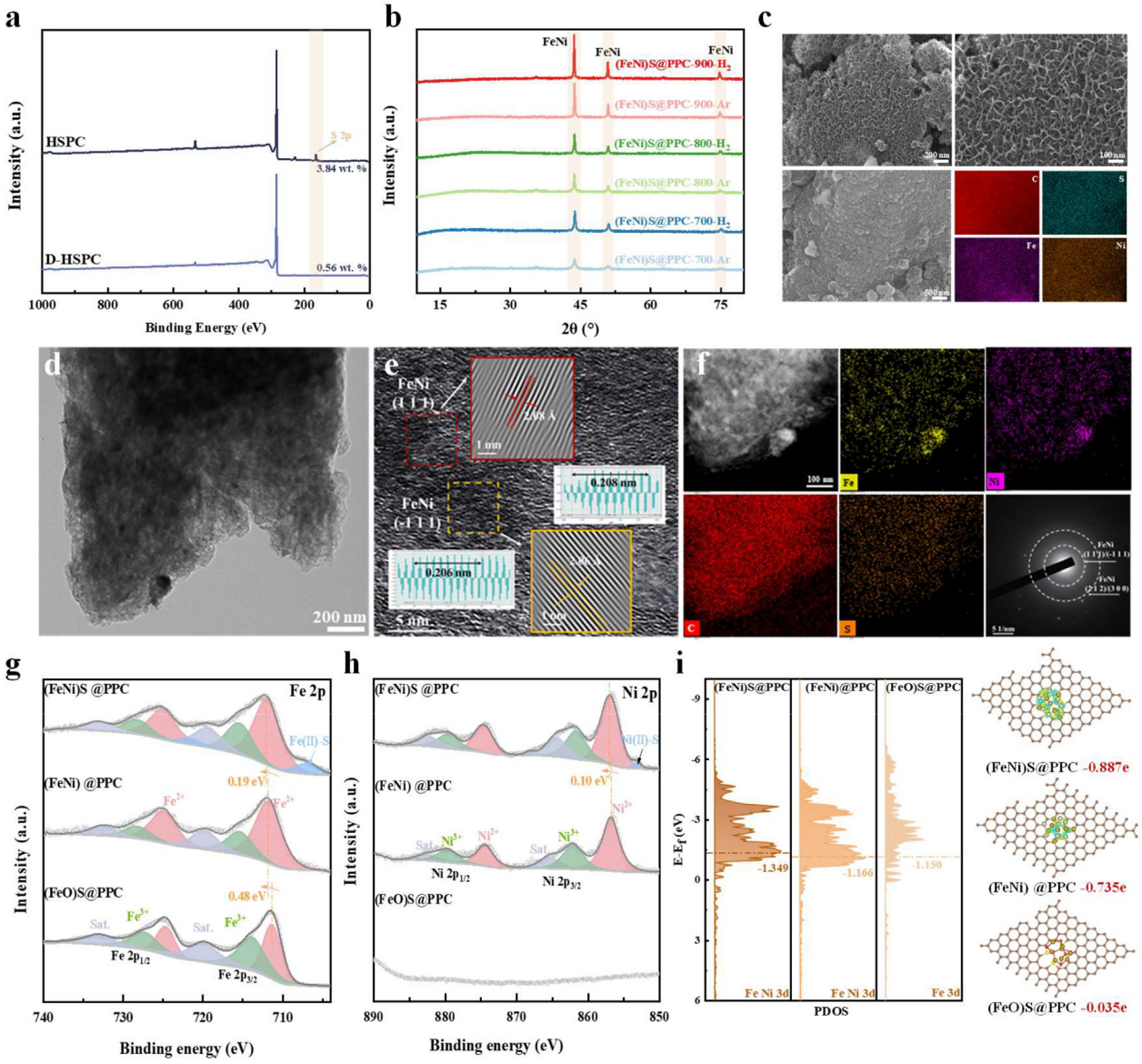

Fig. 2. (a) XPS spectra recorded for the carbon precursors. (b) XRD spectra for the (FeNi)S@PPC. (c–f) SEM, TEM, and EDS results obtained for (FeNi)S@PPC. XPS spectra recorded for the (g) Fe 2p and (h) Ni 2p components. (i) Theoretical modeling and electronic properties of the (FeNi)S@PPC, (FeNi)@PPC, and (FeO)S@PPC systems.

terplanar spacings of 2.06 and 2.08 Å, corresponding to the (−111) and (111) crystallographic planes of the FeNi phase, respectively. Moreover, the selected area electron diffraction (SAED) patterns were found to exhibit distinct diffraction rings assignable to the (−111)/(111) and (212)/(300) crystal planes of FeNi.

The electronic states of Fe and Ni in the (FeNi)S@PPC, (FeNi)@PPC, and (FeO)S@PPC composites were subsequently elucidated using XPS (Fig. 2g–h and Table S4), as were their electronic interactions with the carbon support. The results indicated that (FeNi)S@PPC exhibited a typical doublet structure corresponding to Fe^{2+} and Fe^{3+}, which was accompanied by characteristic satellite peaks. Fe(II)–S (7.16%) was detected in (FeNi)S@PPC, suggesting the existence of sulfur-mediated iron coordination. Notably, the Fe $2p_{3/2}$ peak exhibited a 0.19 eV positive binding energy shift relative to (FeNi)@PPC. This phenomenon can be attributed to the sulfur atoms acting as electron acceptors within the Fe-S-C interface, thereby reducing the electron density around the Fe centers and increasing their apparent oxidation state. The characteristic Ni(II)–S peaks observed at 853.40 and 868.21 eV in the Ni 2p spectrum further confirmed the synergistic coordination effect of FeNi-S. The infrared sulfur analyzer measurements showed that the absolute sulfur content in (FeNi)S@PPC was 4.18 wt.% and in (FeNi)@PPC was 0.43 wt.%, further supporting the above conclusions. Further analysis of the S 2p spectrum (Fig. S8) revealed that (FeNi)S@PPC contained a higher proportion of C-S-C (52.94%), which enhanced the in-

terfacial interactions between the FeNi alloy and the carbon support, thereby regulating the catalytic behavior of the FeNi active centers through electronic effects.

Subsequently, theoretical models were constructed for the three samples by loading Fe_8Ni_8 and Fe_8O_6 clusters onto sulfur-doped and undoped carbon supports. From the calculated differential charge-density maps (Fig. 2i), it was evident that in the case of (FeNi)S@PPC, sulfur doping resulted in a notable accumulation (yellow region) of electronic charges at the interface between FeNi and the carbon support. This phenomenon is consistent with the changes in the d-orbital electron distribution of FeNi in the partial density of states (PDOS), further confirming that sulfur doping enhances the electronic interaction between the metals and the support. The D-band centers for (FeNi)S@PPC, (FeNi)@PPC, and (FeO)S@PPC were located at −1.349, −1.166, and −1.150 eV, respectively. The significant downshift of the D-band center in (FeNi)S@PPC can be attributed to the differences in the electronic properties of sulfur and carbon, which leads to a redistribution of the electronic density around the FeNi cluster. According to the D-band theory, a downshift in the D-band center typically weakens the adsorption strength of reactants on the catalyst surface, thereby reducing the energy barrier for catalytic dehydrogenation and hydrogenation.

3.3. General synthesis and assessment of (FeTM)S@PPC catalysts

Typical 3d TMs, namely Cr, Mn, Co, Ni, and Cu, were investigated as candidate second-metal source dopants under the same conditions. XRD and SEM were used to analyze the crystal phase structures and morphologies of the (FeTM)S@PPC catalysts. More specifically, the XRD patterns (Fig. 3a and b) indicated that while Fe forms solid solutions with Co, Ni, and Cu, the incorporation of Cr and Mn predominantly generates Cr-O and Mn_xO_y (MnO and Mn_3O_4) owing to differences in the thermodynamic affinities of the different elements toward oxygen. SEM images (Fig. S9) revealed that, unlike the layered array structure of (FeNi)S@PPC, the other systems were mainly composed of metal particles dispersed within the carbon matrix. Furthermore, Brunauer–Emmett–Teller (BET) surface area analysis (Fig. 3c) indicated that the (FeNi)S@PPC sample possessed the highest specific surface area (373.69 $m^2 \cdot g^{-1}$), which was significantly greater than that of the other FeTM systems.

Fig. 3d and e presented the isothermal hydrogen desorption curves of the MgH_2 catalyzed by (FeTM)S@PPC at 300 and 275 °C, respectively. It can be seen that (FeNi)S@PPC exhibited superior catalytic dehydrogenation rates at both temperatures, followed by (FeMn)S@PPC. As illustrated in Fig. 3f, the dehydrogenation rates at 275 and 300 °C over 20 min clearly establish the activity sequence: FeNi > FeMn > FeCu > FeCr > FeCo. Based on these results, the comprehensive catalytic hydrogen storage performance and underlying mechanism of (FeNi)S@PPC were subsequently analyzed.

Table 1
Summary of the kinetic activation energy obtained for the (FeNi)S@PPC, (FeNi)@PPC, (FeO)S@PPC, and pure MgH_2 species.

	Samples	Activation energy ($kJ \cdot mol^{-1}$)
Desorption	(FeNi)S@PPC	97.09
	(FeNi)@PPC	102.23
	(FeO)S@PPC	170.78
	pure MgH_2	143.19
Absorption	(FeNi)S@PPC	24.72
	(FeNi)@PPC	25.37
	(FeO)S@PPC	37.78
	pure MgH_2	64.10

3.4. Hydrogen absorption/desorption and cycle stability analysis

To investigate the effects of (FeNi)S@PPC, (FeNi)@PPC, and (FeO)S@PPC on the hydrogen absorption and desorption kinetics of MgH_2, isothermal desorption (Fig. 4a–c) and absorption (Fig. 4d–f) kinetic tests were conducted at various temperatures. Compared with the pure ball-milled MgH_2 (Fig. S10), the hydrogen desorption rates were significantly enhanced for (FeNi)S@PPC and (FeNi)@PPC. At 275 °C, (FeNi)S@PPC released 4.89 wt.% hydrogen within 20 min, achieving 75% of its maximum desorption capacity. This performance was superior to that achieved by the (FeNi)@PPC (3.48 wt.%) and (FeO)S@PPC (0.30 wt.%) catalysts at the same time point (Fig. S11). Meanwhile, the dehydrogenation kinetics of the (FeNi)S@PPC/MgH_2 system were comparable to those reported for representative Mg-based hydrogen storage materials in recent years (Table S5). Additionally, Fig. 4d–f presented the isothermal hydrogenation profiles, demonstrating that (FeNi)S@PPC exhibited an outstanding low-temperature hydrogenation capacity. For instance, at 75 °C, (FeNi)S@PPC absorbed 3.63 wt.% hydrogen within 60 min, significantly exceeding the capacities of (FeNi)@PPC (2.37 wt.%) and (FeO)S@PPC (1.03 wt.%). The activation energies for desorption and absorption were subsequently determined using the Arrhenius equation (Fig. S12). As summarized in Table 1, (FeNi)S@PPC exhibited notably low activation energies of 97.09 $kJ \cdot mol^{-1}$ for desorption and 24.72 $kJ \cdot mol^{-1}$ for absorption, thereby demonstrating the high catalytic activity of this system. Although (FeO)S@PPC exhibited a slightly higher activation energy than ball-milled MgH_2, its dehydrogenation kinetics were superior because the reaction rate was governed by both the activation energy and the pre-exponential factor. Owing to its porous carbon framework and highly dispersed active species, (FeO)S@PPC showed a much larger pre-exponential factor (2.20×10^{12} s^{-1}) than ball-milled MgH_2 (2.53×10^{9} s^{-1}), resulting in a higher reaction rate constant and enhanced dehydrogenation performance.

The cycling stability of the (FeNi)S@PPC/MgH_2 composite was subsequently evaluated over 30 cycles at 325 °C (Fig. 4g). Overall, the system demonstrated excellent long-term stability, with no significant degradation in hydrogen

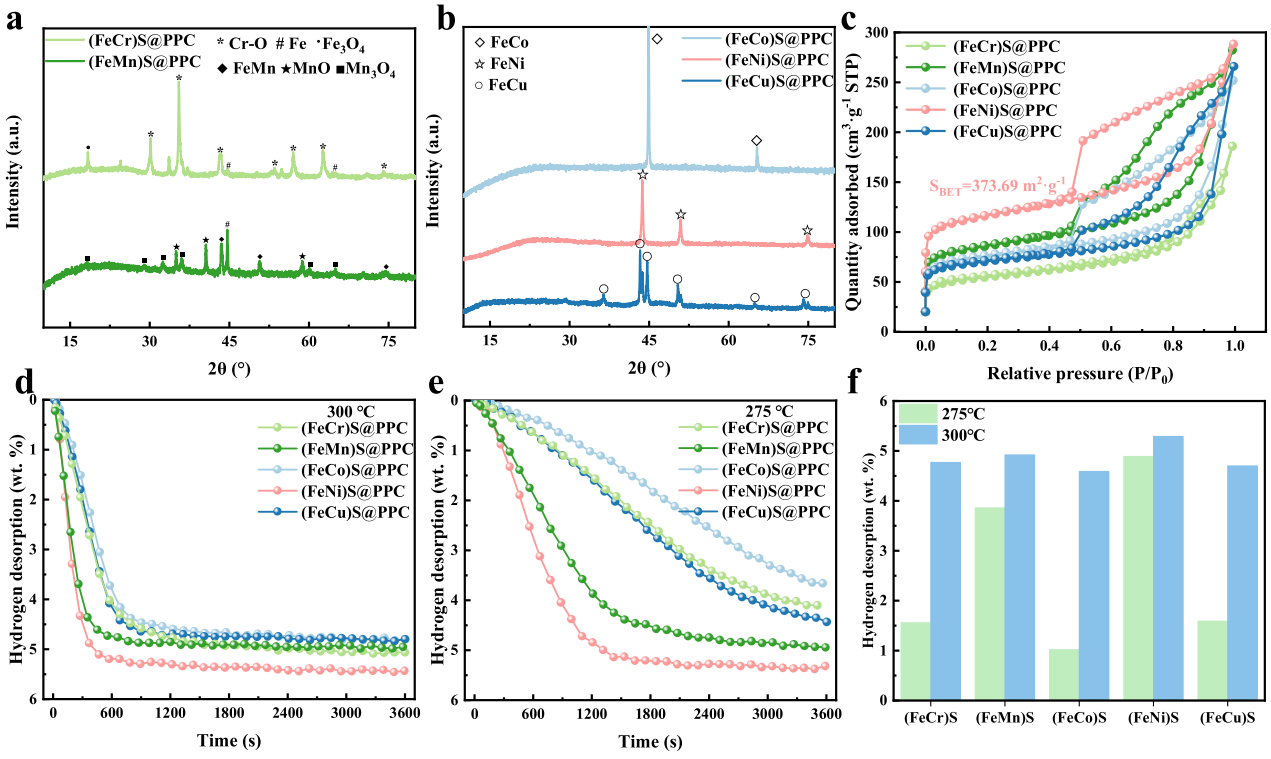

Fig. 3. (a, b) XRD characterization. (c) N_2 adsorption and desorption profiles. Isothermal hydrogen desorption profiles recorded at (d) 300 °C and (e) 275 °C. (f) Comparison of dehydrogenation rates within 20 min across different systems.

storage capacity after 30 cycles. The initial increase in hydrogen storage capacity during the first three cycles originates from an activation process that involves structural optimization and the gradual exposure of active sites, facilitating hydrogen diffusion and activating previously inaccessible reactive sites. The detailed desorption profiles for the representative 5th, 10th, 20th, and 30th cycles are presented in Fig. 4h, where the four curves show high agreement with no discernible performance hysteresis. The (FeNi)S@PPC/MgH_2 showed 99.5% capacity retention after 30 cycles, indicating excellent cycling stability (Fig. 4i). This robust cycling stability was partially ascribed to the activation-induced transformation of the Ni component within (FeNi)S@PPC during initial cycling. XRD analysis (Fig. 5h) confirmed the in situ formation of Mg_2Ni phases, resulting in enhanced kinetics and superior hydrogen capacity in subsequent cycles. In addition, it has been previously demonstrated that carbon can further improve the cycling stability of such materials [51–54].

Furthermore, to elucidate the mechanism by which (FeNi)S@PPC promotes the reaction kinetics, the hydrogen release curves of the three catalysts were fit using nine kinetic models (Table S6) to determine their rate-limiting steps, as shown in Fig. 5a–c. Differences were observed in the rate-limiting steps of the three catalysts, with hydrogen desorption from (FeNi)S@PPC closely following the R3 model (slope = 0.9896), indicating a phase boundary-controlled reaction following a shrinking-core mechanism. In this regime, hydrogen desorption requires overcoming an interfacial energy barrier, wherein three-dimensional diffusion proceeds concurrently with interfacial reactions, and the progressive movement of the interface dictates the reaction rate. In contrast, (FeNi)@PPC exhibited D3 model kinetics, signifying that three-dimensional bulk diffusion through the lattice was the rate-limiting process. Moreover, the (FeO)S@PPC kinetics were best described by the F1 model, implying that the surface chemical processes involved in the breakage/formation of the H–H bonds were the primary kinetic barriers. It was therefore inferred that metal–sulfur bonds between FeNi and the sulfur atoms in (FeNi)S@PPC facilitate transition of the rate-limiting step to a low-energy barrier three-dimensional interface reaction, with desorption occurring along the spherical three-dimensional shrinking reaction interface, thereby improving the hydrogen absorption and desorption kinetics.

Fig. 5d provides a quantitative analysis of the thermodynamic characteristics of (FeNi)S@PPC, specifically regarding the PCT curves recorded at 275, 300, 325, and 350 °C. Each isotherm exhibited a single distinct pressure plateau corresponding to the transformation between MgH_2 and Mg, confirming that the Mg/MgH_2 transformation was the sole detectable hydrogen storage mechanism. The van't Hoff plot (Fig. 5g), derived from the plateau pressures at the corresponding temperatures (Table S7), enabled the determination of the thermodynamic parameters for hydrogen absorption and desorption. Compared to the bulk Mg, the enthalpies of both hydrogen absorption and desorption exhibited a modest decrease in the presence of (FeNi)S@PPC. Specifically, the desorption enthalpy was 75.98 kJ·mol^{-1}, a reduction

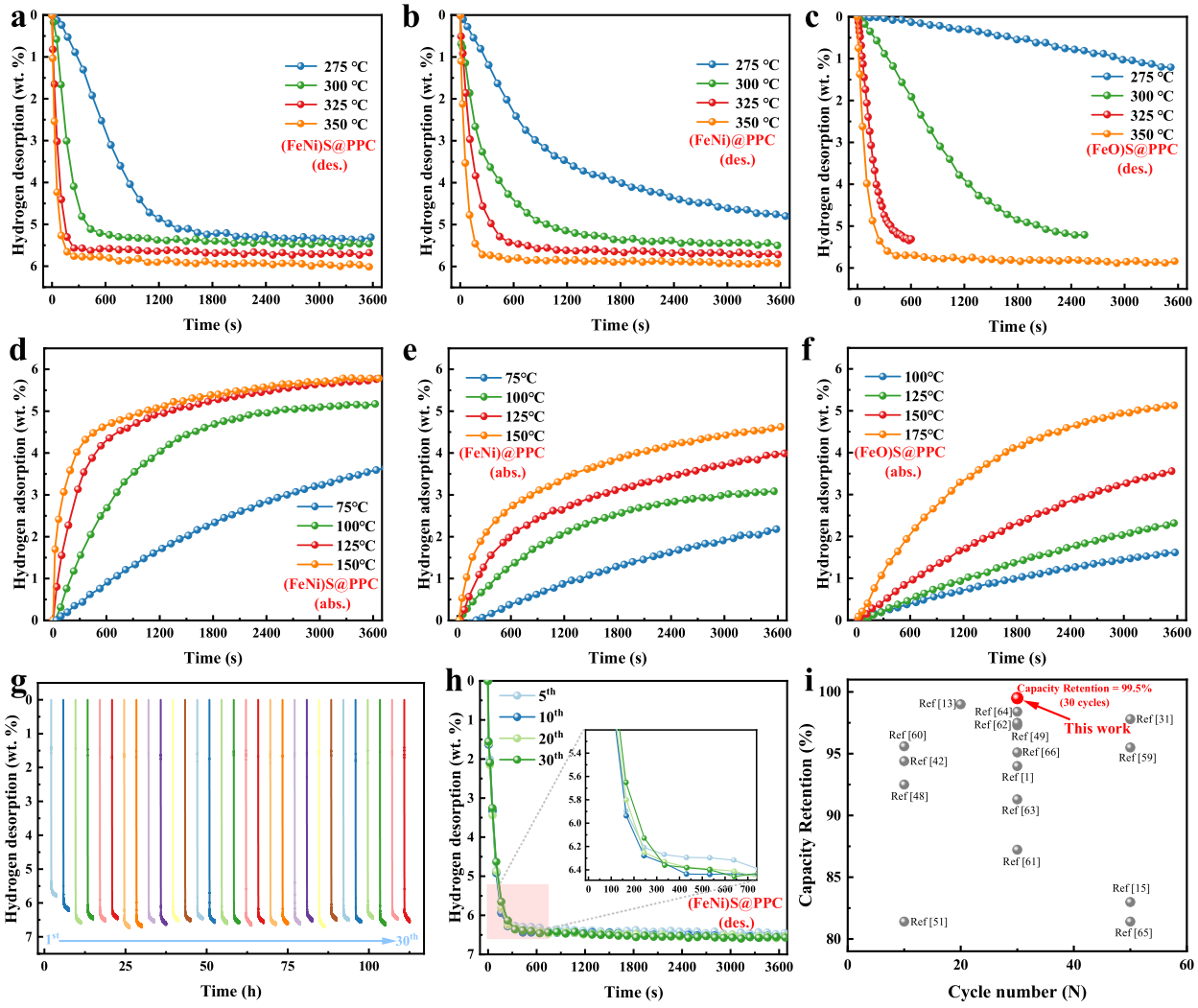

Fig. 4. (a–c) Hydrogen desorption kinetics of MgH_2 catalyzed by (FeNi)S@PPC, (FeNi)@PPC, and (FeO)S@PPC. (d–f) Hydrogen absorption kinetics of MgH_2 catalyzed by (FeNi)S@PPC, (FeNi)@PPC, and (FeO)S@PPC. (g) Isothermal dehydrogenation cycling curves of (FeNi)S@PPC measured at 325 °C for 120 min under 0.001 MPa H_2. (h) Hydrogen desorption kinetics for (FeNi)S@PPC for different cycle numbers. (i) Comparison of hydrogen capacity retention of this work relative to representative studies reported in the literature [1,13,15,38,44,45,47,55–66].

of ~6.18 kJ·mol^{-1} from the 82.16 kJ·mol^{-1} observed for the ball-milled MgH_2 [20]. This reduction was primarily attributed to the (FeNi)S@PPC catalyzed weakening of the Mg–H bond strength, in conjunction with the formation of a low-enthalpy Mg_2NiH_4 phase. Furthermore, structurally destabilizing confinement effects arise from partial carbon encapsulation of MgH_2, as evidenced by TEM diffraction patterns (Fig. 5f).

The specific phase transitions that occur in the (FeNi)S@PPC catalyst during hydrogen absorption and desorption are crucial for defining the catalytic process. To investigate this further, the ball-milled samples, along with those after the first desorption and rehydrogenation processes, were characterized by XRD and XPS, as shown in Fig. 5h–i and S13. The XRD patterns revealed transformations of MgH_2 and Mg throughout cycling, with limited Ni redistribution from (FeNi)S@PPC, facilitating the nucleation of the Mg_2Ni phase at 2θ values of 20.13° and 39.98° Following rehydrogenation, the hydride Mg_2NiH_4 peak was detected at 41.42°, indicating that Mg_2Ni/Mg_2NiH_4 served as a "hydrogen pump" during hydrogen absorption and desorption. Mg_2Ni established rapid hydrogen diffusion pathways and nucleation sites for Mg/MgH_2, thereby accelerating reaction kinetics. Moreover, a certain percentage of FeNi alloy underwent conversion to Fe_7Ni_3 (2θ = 44.76°) due to alloying Ni species with Mg during the catalytic process. The partial structural evolution preserves the stable FeNi-S coordination environment, as evidenced by the invariant of M-S peaks at 161.4 eV ($2p_{3/2}$) and 162.5 eV ($2p_{1/2}$) in deconvoluted S 2p XPS spectra throughout cycling (Fig. 5i). MgS formation was conclusively ruled out by the absence of corresponding XRD diffraction peaks and TEM lattice fringes, further confirming the thermodynamic stability of the FeNi-S coordination configuration on the carbon support.

TEM analysis and corresponding SAED patterns (Fig. 6) revealed the phase evolution of Mg/MgH_2 and

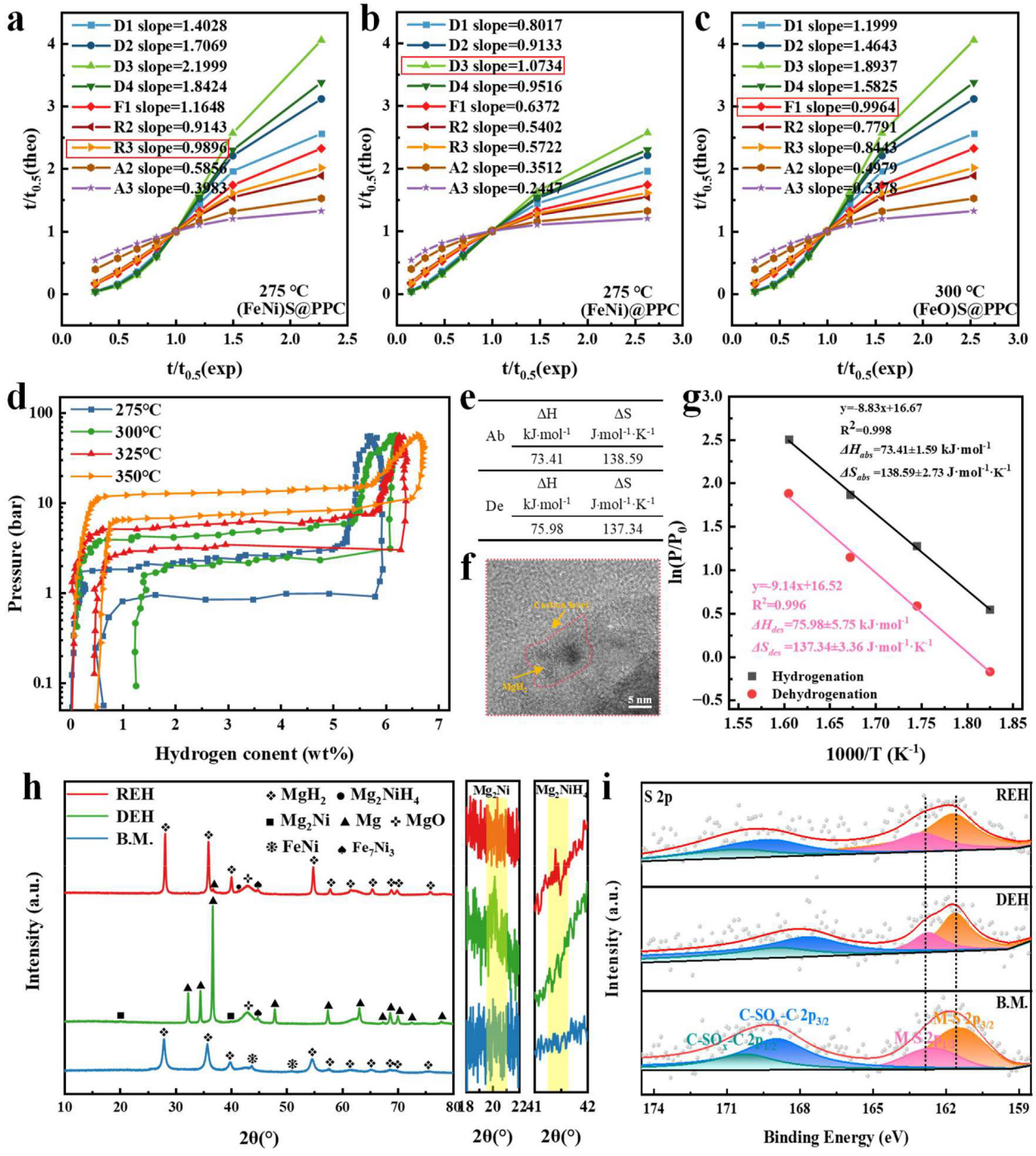

Fig. 5. (a–c) Kinetic models for the MgH_2 dehydrogenation catalyzed by (FeNi)S@PPC, (FeNi)@PPC, and (FeO)S@PPC. (d) PCT for the (FeNi)S@PPC/MgH_2. (e) Thermodynamic parameters for the (FeNi)S@PPC/MgH_2. (f) TEM image of MgH_2 encapsulated by a carbon layer. (g) Van't Hoff plots of (FeNi)S@PPC/MgH_2. (h, i) XRD and XPS obtained for the ball-milled, dehydrogenated, and rehydrogenated (FeNi)S@PPC/MgH_2.

Mg_2Ni/Mg_2NiH_4 hydrides during cycling, concurrently detecting FeNi and Fe_7Ni_3 alloy phases. The EDS images indicated uniform distributions of C, S, Fe, and Ni across the Mg/MgH_2 particles. XRD, XPS, and HAADF-STEM results showed that the (FeNi)S@PPC catalyst retained FeNi–S structural integrity to establish stable catalytic activity for MgH_2 during cycling, with limited generation of Mg_2Ni providing nucleation sites and hydrogen diffusion channels. Sulfur doping of the carbon support facilitated pivotal catalytic actions via FeNi–S bonds, as elucidated in the subsequent section using DFT calculations.

3.5. Microscopic mechanism of FeNi–S for enhancing Mg/MgH_2 performance

To gain a deeper understanding of the mechanism by which FeNi–S coordination in (FeNi)S@PPC enhances the hydrogen storage performance of MgH_2 at the microscopic electronic

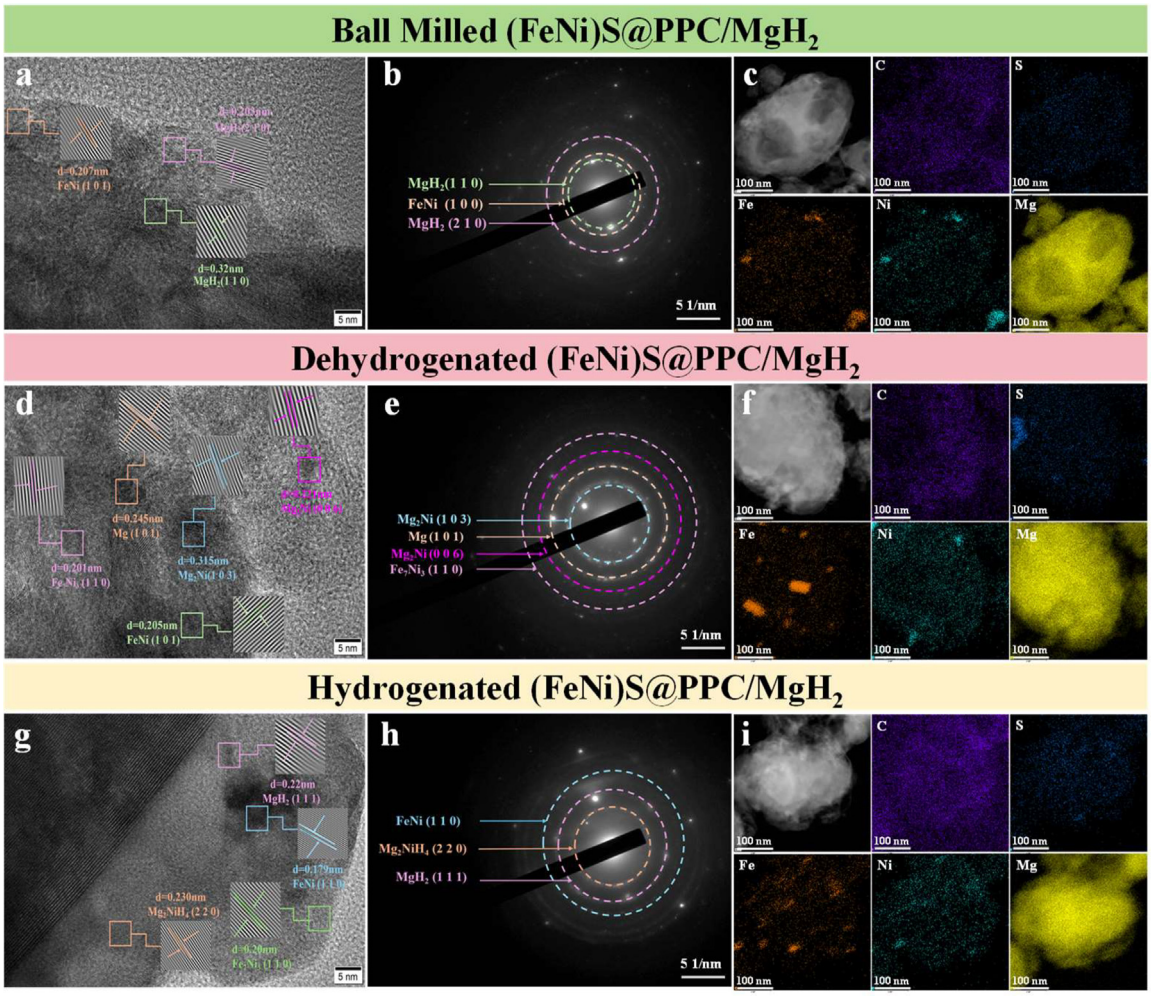

Fig. 6. TEM, HRTEM, and EDS of (FeNi)S@PPC/MgH_2 system after ball milling, dehydrogenation, and rehydrogenation.

level, DFT calculations were performed to simulate the interactions between H_2 and MgH_2 with the catalytically active sites of (FeNi)S@PPC. Considering their distinct catalytic adsorption sites, two catalytic models were constructed based on (FeNi)S@PPC and (FeNi)@PPC. The calculated adsorption energies of H_2, as shown in Fig. 7a, indicated that both (FeNi)S@PPC and (FeNi)@PPC exhibited stable chemical adsorption, with adsorption energies of −1.36 and −1.90 eV, respectively. In the stable adsorption configuration, the two H atoms of H_2 approached a dissociated state and formed bonds with either Fe or Ni, indicating that the dissociation of H_2 was not the rate-determining step in this process. Moreover, the hydrogen adsorption strength of (FeNi)S@PPC was lower than that of (FeNi)@PPC. The calculated PDOS corroborated this finding, as shown in Fig. 7d, which revealed significant hybridization between the s orbitals of H and the s and d orbitals of Fe and Ni in the range from −10 to −5 eV, with a higher hybridization intensity in the (FeNi)@PPC model.

Notably, H atoms formed by H_2 dissociation must further diffuse into the bulk Mg phase to complete the hydrogenation process. Excessively strong Ni–H or Fe–H interactions can therefore lead to an overly stable hydrogen dissociative state, resulting in a high energy requirement for diffusion. Fig. 7b–c illustrates the diffusion process of H atoms adsorbed and dissociated from the FeNi sites into the Mg cluster, enabling the determination of the kinetic energy barriers and reaction energies required for this process. The highly stable FeNi–(H) bonds in (FeNi)@PPC lead to a higher hydrogen diffusion energy barrier (0.99 eV). In contrast, the appropriately balanced FeNi–(H) interactions in (FeNi)S@PPC reduced the hydrogen diffusion energy barrier to 0.60 eV, thereby accounting for its enhanced hydrogenation kinetics relative to (FeNi)@PPC. In contrast, (FeO)S@PPC exhibited poor catalytic performance due to its weak hydrogen adsorption (–0.12 eV), which ultimately increased the dissociation energy barrier. Notably, no electron cloud overlap between H_2 and (FeO)S@PPC was observed at identical isosurface levels (Fig. S14). Similarly, H_2 dissociation on the pure Mg (Fig. 7b and Fig. S15) exhibited a substantially higher activation energy (1.85 eV), confirming that catalytic modification was crucial for facilitating hydrogenation on magnesium.

The desorption mechanism was also evaluated by calculating the stable adsorption of Mg_4H_8 on (FeNi)S@PPC and (FeNi)@PPC using the optimized geometric structure shown

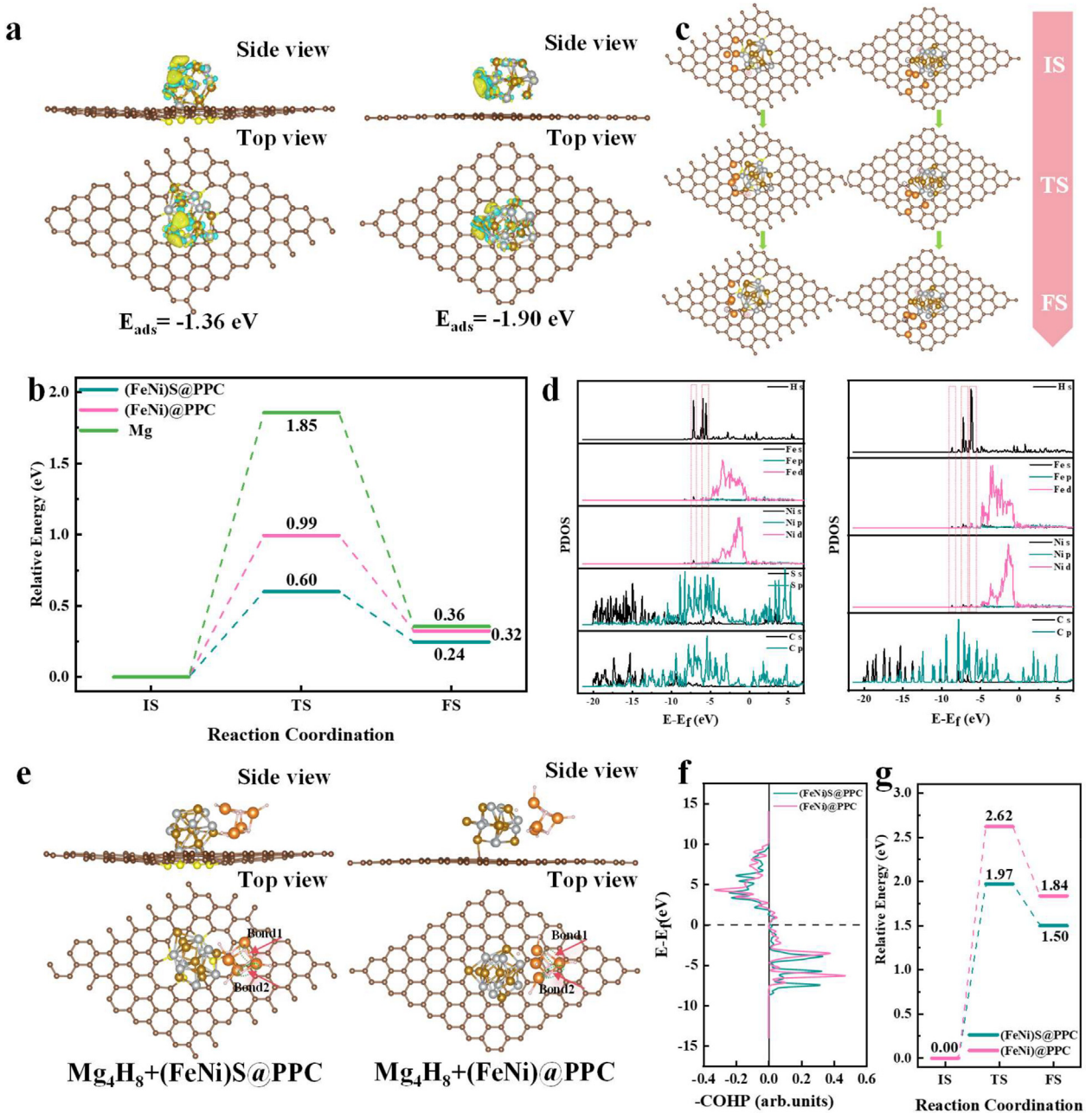

Fig. 7. (a) Charge transfer distributions of H_2 adsorption on the (FeNi)S@PPC (Left) and (FeNi)@PPC (Right). (b, c) Activation energies and reaction pathways of hydrogen dissociation/diffusion. (d) Calculated PDOS for H_2 adsorption on the (FeNi)S@PPC (Left) and (FeNi)@PPC (Right). (e) Optimized stable structures of Mg_4H_8 adsorbed on the (FeNi)S@PPC and (FeNi)@PPC surfaces. (f) Calculated COHP results for Mg–H. (g) Activation energies and barriers associated with the dissociation of Mg–H to form H_2.

in Fig. 7e. It should be noted that in this work, the Mg_4H_8 cluster was employed as a representative unit of MgH_2 to capture the key local Mg–H interactions. Under the same computational conditions, using this model to analyze the effect of sulfur coordination on dehydrogenation comparatively is both reasonable and meaningful. Analysis of the Mg–H bonding strength within the Mg_4H_8 cluster revealed that weaker Mg–H bonding orbitals below 0 eV for (FeNi)S@PPC than for (FeNi)@PPC, as evidenced by COHP curves (Fig. 7f). This reduced bond strength facilitates Mg–H cleavage and subsequent dehydrogenation. Figs. 7g and S16 illustrated the energy barriers and reaction energies associated with the dissociation of Mg–H to form H_2. The energy barrier for hydrogen desorption catalyzed by (FeNi)S@PPC was 1.97 eV, while (FeNi)@PPC possessed a higher barrier of 2.62 eV. These results further confirmed that the self-doping of sulfur into the carbon support significantly lowered the D-band center of (FeNi)S@PPC, resulting in a redistribution of the electron density around FeNi and an increase in the apparent valence state. These lead to a reduction in the FeNi–(H) bond and to a weakening of the Mg–H bond strength, thereby optimizing hydrogen dissociation and diffusion.

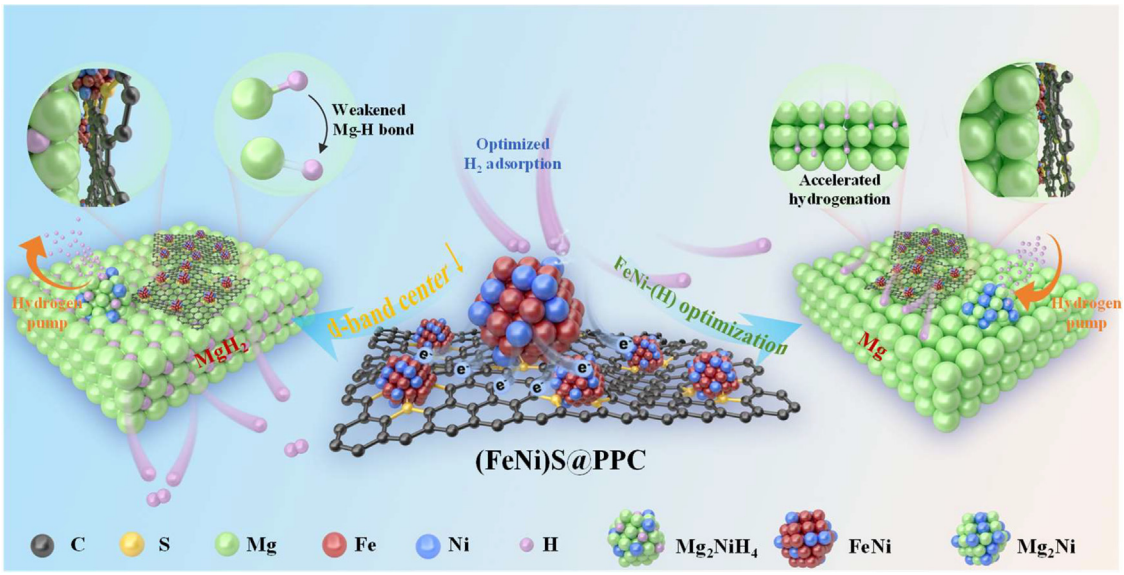

Fig. 8. Schematic representation showing the dehydrogenation/hydrogenation mechanisms of the MgH_2 system over the (FeNi)S@PPC catalyst.

Finally, a schematic representation of the mechanism of enhanced Mg/MgH_2 kinetic and cycling properties catalyzed by (FeNi)S@PPC was constructed based on the above discussions, as shown in Fig. 8. (FeNi)S@PPC maintains the stable coordination environment of FeNi–S during the dehydrogenation/hydrogenation processes, thereby providing stable catalytic active sites of FeNi and Fe_7Ni_3. The electronic structure of the active centers is redistributed through charge transfer between FeNi–S on the carbon support. This redistribution facilitates hydrogen dissociation and diffusion by forming FeNi–(H) bonds with moderate strength. Concurrently, the downshifted D-band center weakens the Mg–H bond, thereby lowering the dehydrogenation energy barriers and enhancing the kinetics. Additionally, the limited Ni redistribution within (FeNi)S@PPC promotes the nucleation of the Mg_2Ni phase, providing rapid diffusion channels and nucleation sites for Mg/MgH_2. Collectively, this work successfully achieves self-doping of HSPC through an improved green activation process, enabling the modulation of the electronic state of the active component and consequently leading to a significant improvement in the hydrogen storage performance of MgH_2.

4. Conclusion

In summary, a high-value transformation of HSPC solid waste was achieved through a green K_2FeO_4 activation strategy, enabling the successful synthesis of sulfur self-doped carbon (FeTM)S@PPC catalysts. The optimal performance of (FeNi)S@PPC was demonstrated, showing advantages over commercial carbon supports in enhancing the hydrogen storage performance of MgH_2. The (FeNi)S@PPC/MgH_2 system exhibited a rapid hydrogen release of 4.89 wt.% within 20 min at 275 °C, surpassing the sulfur-free control system (FeNi)@PPC by 1.41 wt.%. Kinetic analysis indicated that this process was controlled by a low-energy barrier three-dimensional interfacial reaction (R3 model). It also achieved a significantly low-temperature hydrogen uptake, absorbing 3.63 wt.% H_2 within 60 min at 75 °C. Combined experimental and theoretical calculations revealed that intrinsic sulfur self-doping stabilized a FeNi–S coordination environment in (FeNi)S@PPC, thereby optimizing the bond strength of the FeNi–(H) intermediate formed during hydrogenation, facilitating hydrogen dissociation and diffusion. Simultaneously, the D-band center of the FeNi active sites shifted down to –1.349 eV, weakening the Mg–H bond and accelerating dehydrogenation. This work not only provides a novel green strategy for the utilization of HSPC solid waste, but also deepens understanding of how local metal–sulfur coordination affects the hydrogen storage mechanism of Mg/MgH_2.

Declaration of competing interest

The authors declare that they have no known competing financial interests or personal relationships that could have appeared to influence the work reported in this paper.

CRediT authorship contribution statement

Yulin Huang: Writing – review & editing, Writing – original draft, Validation, Software, Methodology, Investigation, Data curation. **Fenghua Wei:** Formal analysis. **Yang Zhang:** Investigation. **Xinan Zhang:** Investigation. **Yiming Wang:** Investigation. **Chen Huang:** Resources. **Yuke Li:** Methodology. **Jingcai Chang:** Writing – review & editing, Funding acquisition.

Acknowledgments

This work was supported by the National Natural Science Foundation of China (22478227), Shandong Provincial Natural Science Foundation (ZR2021ME049), and Taishan Indus-

trial Experts Program (TSCX202306135). The authors thank the Qingda Low Carbon Green Hydrogen Industrial Technology Research Institute Experimental Test Center and Qingdao Haitai Energy Science and Technology Research Institute for experimental characterization.

Supplementary materials

Supplementary material associated with this article can be found, in the online version, at doi:10.1016/j.jma.2026.102033.

References

[1] H. Guan, J. Liu, Q. Li, Y. Lu, F. Pan, J. Magnes. Alloy. (2025) 101708, doi:10.1016/j.jma.2025.02.032.
[2] K. Jeon, H.R. Moon, A.M. Ruminski, B. Jiang, C. Kisielowski, R. Bardhan, J.J. Urban, Nat. Mater. 10 (2011) 286–290, doi:10.1038/nmat2978.
[3] Y. Fu, L. Zhang, Y. Li, S. Guo, H. Yu, W. Wang, K. Ren, W. Zhang, S. Han, J. Magnes. Alloy. 11 (2023) 2927–2938, doi:10.1016/j.jma.2021.11.033.
[4] H. Oh, N. Tumanov, V. Ban, X. Li, B. Richter, M.R. Hudson, C.M. Brown, G.N. Iles, D. Wallacher, S.W. Jorgensen, L. Daemen, R. Balderas-Xicohtencatl, Y. Cheng, A.J. Ramirez-Cuesta, M. Heere, S. Posada-Perez, G. Hautier, M. Hirscher, T.R. Jensen, Y. Filinchuk, Nat. Chem. 16 (2024) 809–816, doi:10.1038/s41557-024-01443-x.
[5] F. Marques, M. Balcerzak, F. Winkelmann, G. Zepon, M. Felderhoff, Energy Environ. Sci. 14 (2021) 5191–5227, doi:10.1039/d1ee01543e.
[6] B. Liu, B. Zhang, H. Huang, X. Chen, Y. Lv, Z. Li, J. Yuan, Y. Wu, J. Magnes. Alloy. 11 (2023) 1815–1824, doi:10.1016/j.jma.2021.08.019.
[7] H. Wang, J. Li, X. Wei, Y. Zheng, S. Yang, Y. Lu, Z. Ding, Q. Luo, Q. Li, F. Pan, Thermodynamic and kinetic regulation for Mg-based hydrogen storage materials: challenges, strategies, and perspectives, Adv. Funct. Mater. 34 (2024) 2406639, doi:10.1002/adfm.202406639.
[8] M.D. Allendorf, V. Stavila, J.L. Snider, M. Witman, M.E. Bowden, K. Brooks, B.L. Tran, T. Autrey, Nat. Chem. 14 (2022) 1214–1223, doi:10.1038/s41557-022-01056-2.
[9] J. Zhang, M. Liu, J. Qi, N. Lei, S. Guo, J. Li, X. Xiao, L. Ouyang, Prog. Mater. Sci. 148 (2025) 101381, doi:10.1016/j.pmatsci.2024.101381.
[10] L. Zeng, Z. Lan, B. Li, H. Liang, X. Wen, X. Huang, J. Tan, H. Liu, W. Zhou, J. Guo, J. Magnes. Alloy. 10 (2022) 3628–3640.
[11] C. Li, W. Yang, H. Liu, X. Liu, X. Xing, Z. Gao, S. Dong, H. Li, Angew. Chem. Int. Ed. 63 (2024) e202320151, doi:10.1002/anie.202320151.
[12] M. Liu, S. Zhao, X. Xiao, M. Chen, C. Sun, Z. Yao, Z. Hu, L. Chen, Nano Energy 61 (2019) 540–549, doi:10.1016/j.nanoen.2019.04.094.
[13] Z. Liu, H. Ning, R. Liu, S. Ding, J. Yang, Y. Tan, Y. Fan, R. Li, P. Qing, H. Liu, J. Guo, Z. Lan, Chem. Eng. J. 499 (2024) 155877, doi:10.1016/j.cej.2024.155877.
[14] H. Guan, Y. Lu, J. Liu, Y. Ye, Q. Li, F. Pan, Acs Catal 14 (2024) 17159–17170, doi:10.1021/acscatal.4c06122.
[15] T. Zhong, T. Xu, L. Zhang, L. Wang, F. Wu, X. Yu, Adv. Funct. Mater. 35 (2025) 2418230, doi:10.1002/adfm.202418230.
[16] J. Hu, W. Jiang, N. Si, Z. Wang, Z. Cao, J. Energy Storage 123 (2025) 116824, doi:10.1016/j.est.2025.116824.
[17] S. Ding, Y. Qiao, X. Cai, H. Wang, X. Shen, L. Xu, Y. Wen, F. Jiang, W. Zhou, T. Shen, J. Magnes. Alloy. 13 (2025) 1341–1352, doi:10.1016/j.jma.2024.04.020.
[18] Q. Hou, J. Wang, Y. Zhou, P. Jiang, Y. Li, Z. Ding, Q. Wang, Y. Xiong, J. Power Sources 640 (2025) 236713, doi:10.1016/j.jpowsour.2025.236713.
[19] J. Zhang, W. Wang, X. Chen, J. Jin, X. Yan, J. Huang, J. Am. Chem. Soc. 146 (2024) 10432–10442, doi:10.1021/jacs.3c13970.
[20] J. Zhang, C. Zheng, Y. Wang, T. Zhai, Y. Zhang, D. Feng, Int. J. Hydrogen Energy 95 (2024) 666–677, doi:10.1016/j.ijhydene.2024.11.016.
[21] S. Liu, Y. Zhang, F. Zhu, J. Liu, X. Wan, R. Liu, X. Liu, J.X. Shang, R. Yu, Q. Feng, Z. Wang, J. Shui, Adv. Sci. 11 (2024) 2401868, doi:10.1002/advs.202401868.
[22] L.F. Wan, Y. Liu, E.S. Cho, J.D. Forster, S. Jeong, H. Wang, J.J. Urban, J. Guo, D. Prendergast, Nano Lett 17 (2017) 5540–5545, doi:10.1021/acs.nanolett.7b02280.
[23] T.W. van Deelen, C. Hernández Mejía, K.P. de Jong, Nat. Catal. 2 (2019) 955–970, doi:10.1038/s41929-019-0364-x.
[24] W. Chen, Y. Che, J. Xia, L. Zheng, H. Lv, J. Zhang, H. Liang, X. Meng, D. Ma, W. Song, X. Wu, C. Cao, Metal–sulfur interfaces as the primary active sites for catalytic hydrogenations, J. Am. Chem. Soc. 146 (2024) 4c–2692c, doi:10.1021/jacs.4c02692.
[25] P. Yin, X. Luo, Y. Ma, S. Chu, S. Chen, X. Zheng, J. Lu, X. Wu, H. Liang, Nat. Commun. 12 (2021) 3135, doi:10.1038/s41467-021-23426-z.
[26] J. Zhang, Z. Li, B. Liu, M. Chen, Y. Zhou, M. Zhu, Appl. Catal. B Environ. 328 (2023) 122522, doi:10.1016/j.apcatb.2023.122522.
[27] X. Wang, C. Zhang, D. Li, Y. Sun, J. Ren, J. Sun, D. Yang, J. Hazard. Mater. 454 (2023) 131469, doi:10.1016/j.jhazmat.2023.131469.
[28] C. Duan, Y. Tian, X. Wang, J. Wu, B. Liu, D. Fu, Y. Zhang, W. Lv, L. Hu, F. Wang, X. Zhang, Y. Wu, Nano Energy 113 (2023) 108536, doi:10.1016/j.nanoen.2023.108536.
[29] K. Wang, X. Zhang, Y. Liu, Z. Ren, X. Zhang, J. Hu, M. Gao, H. Pan, Chem. Eng. J. 406 (2021) 126831, doi:10.1016/j.cej.2020.126831.
[30] G. Kresse, Phys. Rev. B 192–193 (1993) 222–229.
[31] B.G. Johnson, P.M.W. Gill, J.A. Pople, J. Chem. Phys. 97 (1992) 7846–7848, doi:10.1063/1.463975.
[32] W. Kohn, Phys. Rev. 140 (1965) A1133.
[33] G. Henkelman, B.P. Uberuaga, H. Jónsson, J. Chem. Phys. 113 (2000) 9901–9904, doi:10.1063/1.1329672.
[34] Y. Chen, X. Li, B. Sun, G. Zhang, S. Ni, C. Li, Int. J. Hydrog. Energy 121 (2025) 326–336, doi:10.1016/j.ijhydene.2025.03.367.
[35] Q. Hou, J. Wang, Y. Zhou, P. Jiang, Y. Li, Z. Ding, Q. Wang, Y. Xiong, J. Power Sources 640 (2025) 236713, doi:10.1016/j.jpowsour.2025.236713.
[36] H. Huang, T. Xu, J. Chen, J. Yuan, W. Yang, B. Liu, B. Zhang, Y. Wu, Chem. Eng. J. 483 (2024) 149434, doi:10.1016/j.cej.2024.149434.
[37] J. Li, R. Zou, Y. Cui, G. Lei, Z. Li, H. Cao, Chem. Eng. J. 470 (2023) 144259, doi:10.1016/j.cej.2023.144259.
[38] Y. Li, L. Ren, Y. Yao, Y. Zhao, H. Xu, Z. Li, Z. Li, X. Dai, Y. Tian, S. Cao, X. Lin, C. Ye, A. Züttel, J. Zou, Adv. Funct. Mater. 35 (2025) 2417915, doi:10.1002/adfm.202417915.
[39] X. Lu, L. Zhang, H. Yu, Z. Lu, J. He, J. Zheng, F. Wu, L. Chen, Chem. Eng. J. 422 (2021) 130101, doi:10.1016/j.cej.2021.130101.
[40] D. Peng, Y. Zhang, S. Han, ACS Sustain. Chem. Eng. 9 (2021) 998–1007, doi:10.1021/acssuschemeng.0c08507.
[41] Y. Qin, J. Hu, Z. Yang, C. Han, S. Long, D. Zhang, Y. Chen, F. Pan, J. Magnes. Alloy. 12 (2024) 4877–4886, doi:10.1016/j.jma.2024.02.012.
[42] L. Ren, Y. Li, Z. Li, X. Lin, C. Lu, W. Ding, J. Zou, Nano-Micro Lett 16 (2024) 160, doi:10.1007/s40820-024-01375-8.
[43] M.F. Saeid, B.A. Abdulkadir, M. Ismail, H.D. Setiabudi, Fuel 400 (2025) 135635, doi:10.1016/j.fuel.2025.135635.
[44] X. Wang, Z. Yuan, Y. Shi, S. Li, G. Mi, Q. Peng, S. Han, Y. Fan, B. Liu, J. Magnes. Alloy. (2025) 101763, doi:10.1016/j.jma.2025.04.029.
[45] Y. Wang, Y. Xia, E. Xu, C. Xiang, X. Qing, Z. Yang, F. Xu, L. Sun, Y.S. Chua, Y. Zou, J. Magnes. Alloy. (2025) 101634, doi:10.1016/j.jma.2024.12.015.
[46] M. Wu, M. Gao, S. Qu, Y. Liu, W. Sun, X. Zhang, C. Liang, X. Zhang, Y. Yang, H. Pan, J. Magnes. Alloy. 13 (2025) 613–625, doi:10.1016/j.jma.2024.03.025.
[47] H. Xiao, L. Yi, H. Lei, Y. Xu, X. Zhang, H. Hu, R. Tang, Q. Li, Q. Chen, J. Magnes. Alloy. 13 (2025) 4206–4218, doi:10.1016/j.jma.2025.01.005.
[48] X. Yang, X. Wang, R. Liu, Y. Liu, Z. Li, W. Cui, F. Qi, Y. Yang, J. Chen, H. Pan, J. Magnes. Alloy. 13 (2025) 6154–6166, doi:10.1016/j.jma.2025.06.014.
[49] Y. Zheng, L. Zhang, H. Zheng, J. Chen, Z. Chen, Y. Liu, J. Tu, C. Gu, J. Colloid. Interface. Sci. 685 (2025) 65–72, doi:10.1016/j.jcis.2025.01.100.

[50] Y. Zhu, Z. Qin, X. Shi, X. Ding, V. Dao, Y. Li, Chem. Eng. J. 498 (2024) 155285, doi:10.1016/j.cej.2024.155285.
[51] X. Xing, X. Zhang, M. Wei, Z. Zhang, B. Cao, T. Liu, Small 20 (2024) 2402982, doi:10.1002/smll.202402982.
[52] X. Lu, L. Zhang, H. Yu, Z. Lu, J. He, J. Zheng, F. Wu, L. Chen, Chem. Eng. J. 422 (2021) 130101, doi:10.1016/j.cej.2021.130101.
[53] X. Lu, L. Zhang, H. Yu, Z. Lu, J. He, J. Zheng, F. Wu, L. Chen, Chem. Eng. J. 422 (2021) 130101, doi:10.1016/j.cej.2021.130101.
[54] Y. Meng, S. Ju, W. Chen, X. Chen, G. Xia, D. Sun, X. Yu, Small Struct 3 (2022) 2200119, doi:10.1002/sstr.202200119.
[55] L. Wang, T. Zhong, F. Wu, D. Chen, Z. Yao, L. Chen, L. Zhang, Chem. Eng. J. 505 (2025) 159591, doi:10.1016/j.cej.2025.159591.
[56] F. Bu, A. Wajid, N. Yang, M. Gu, X. Zhao, L. Huang, X. Ji, S. Ding, Y. Cheng, J. Zhang, J. Mater. Chem. A 12 (2024) 12190–12197, doi:10.1039/d4ta00722k.
[57] C. Li, Y. Ding, X. Zhang, X. Hu, X. Yu, D. Sun, G. Xia, Adv. Mater. 37 (2025) e11759, doi:10.1002/adma.202511759.
[58] H. Lu, J. Li, X. Zhou, Y. Lu, Y. Chen, Q. Li, F. Pan, J. Mater. Sci. Technol. 190 (2024) 135–144, doi:10.1016/j.jmst.2023.11.056.
[59] Z. Yang, Y. Wang, X. Lin, Y. Zou, C. Xiang, F. Xu, L. Sun, Y.S. Chua, J. Magnes. Alloy. 13 (2025) 4020–4031, doi:10.1016/j.jma.2025.01.012.
[60] Z. Yang, W. Sun, Y. Bu, R. Zhang, Z. Yang, B. Li, L. Sun, F. Xu, T. Yu, W. Guo, Y. Liu, Z. Liang, Chem. Eng. J. 522 (2025) 167955, doi:10.1016/j.cej.2025.167955.
[61] T. Zhang, M. Liu, C. Li, J. Zhang, H. Gao, F. Kong, X. Xiao, Chem. Eng. J. 511 (2025) 162185, doi:10.1016/j.cej.2025.162185.
[62] X. Zhou, H. Guan, H. Lu, Y. Lu, J. Li, J. Wang, Y. Chen, Q. Li, F. Pan, J. Magnes. Alloy. 13 (2025) 571–582, doi:10.1016/j.jma.2023.09.016.
[63] Z. Yu, X. Liu, Y. Liu, Y. Li, Z. Zhang, K. Chen, S. Han, Fuel 357 (2024) 129726, doi:10.1016/j.fuel.2023.129726.
[64] T. Zhang, M. Liu, C. Li, J. Zhang, H. Gao, F. Kong, X. Xiao, Chem. Eng. J. 511 (2025) 162185, doi:10.1016/j.cej.2025.162185.
[65] Y. Huang, J. Chang, Y. Zhang, X. Zhang, Y. Wang, H. Wu, C. Xu, C. Huang, Z. He, Fuel 389 (2025) 134568, doi:10.1016/j.fuel.2025.134568.
[66] L. Ren, Y. Li, Z. Li, X. Lin, C. Lu, W. Ding, J. Zou, Nano-Micro Lett 16 (2024) 160, doi:10.1007/s40820-024-01375-8.